Research on 3D Density Imaging Method with Gravity and Gravity Gradient in the Wavenumber Domain

Huiyou He[1], Jian Fang[1*],Dongmei Guo[1], Ronghua Cui[1], Zhixin Xue[1,2]

[1] State Key Laboratory of Geodesy and Earth's Dynamics, Innovation Academy for Precision Messurement Science and Technology, Chinese Academy of Sciences, 340 Xudong Road, Wuhan 430077, China

[2] University of Chinese Academy of Sciences, No. 19A Yuquan Road, Beijing 100049, China

* Corresponding author at: Jian Fang(jfang@whigg.ac.cn)

Key Points:

- The characteristics of gravity/gravity gradient and their spectrum were analyzed.
- Gravity/gravity gradient reflecting different depths was used for density imaging.
- A High-precision 3D density model was obtained quickly in the wavenumber domain.

Abstract: Density imaging is a method of inverting the sub-surface density distribution according to the spectrum of the gravity and gravity gradient in the wavenumber domain. This method effectively gives full play to the characteristics of fast calculation in the wavenumber domain, improves the computation efficiency, and creates an accurate 3D sub-surface density model. In this paper, the corresponding relation between the gravity and gravity gradient anomalies and the model, and their spectral characteristics were analyzed, which according to preliminary inverse. Then, the 3D density imaging of gravity and gravity gradient was performed on the theoretical data and its noise-added data in the wavenumber domain with depth weighing, and a density model consistent with the theoretical model was obtained. The strong anti-noise capacity of the density imaging method was proved. Finally, the method was verified in the Decorah area of the United States, and the characteristics of gravity and gravity gradient anomalies measured in this area were analyzed, and the 3D density imaging of gravity and gravity gradient was performed in the wavenumber domain. The location of the siliceous intrusive rocks with the relatively low-density and the Decorah complex with the relatively high-density, and the intrusive rock mass with the relatively high-density distributed in the surrounding rock were obtained through inversion. A clear understanding of the intrusive pathways to the rock mass was obtained, and the effectiveness of the density imaging method has been verified. This provides support for further understanding of the structural division and geological evolution in this area.
Keywords: gravity gradient, wavenumber domain, forwarding modeling, density imaging, inversion

1. Introduction

Gravity and gravity gradient data provide the main source for studying the earth's structure and mineral resources. Conventional gravity prospecting observes the gravity anomaly data. In recent years, increasing high-precision gravity gradient data have been obtained due to technological development. Gravity gradient is the first- order derivative of the gravity anomaly, and reflects the high-frequency information. Gravity anomalies contain a lot of low-frequency information. Accurate sub-surface

information can be obtained through analysis of both gravity and gravity gradient anomalies. The earth gravity field provides a geophysical method for studying the internal structure of the earth and searching for mineral resources, and the geological problems are solved based on the gravity anomaly due to the uneven density distribution of geological structures and mineral resources. Gravity anomalies reflect abundant information on the distribution of materials inside the earth. Therefore, the gravity prospecting method plays a significant role in the prospecting of the earth's structure, oil and gas and mineral resource exploration, regional geological survey, archaeological exploration, hydrological and engineering geological survey(Martinez et al., 2010; Vasco and Taylor, 1991). The gravity gradient is the change rate of the first-order derivative of the gravity potential in three directions, and it is the second-order derivative of the gravity potential. In the derivation process, the high-frequency signal is enhanced, and the low-frequency signal is suppressed. Compared with gravity anomaly, gravity gradient anomaly reflects more high-frequency information and provides a higher resolution for shallow anomaly and sudden variation in field source boundaries. The accuracy of geological interpretation can be improved through the integrated utilization of various gradient information. In the past, conventional gravity measurement can only observe the vertical first-order derivative of gravity. With the increasing progress of gravity observation methods, the high-precision gravity gradient observation data can be obtained with the full tensor gravity gradient measurement system (FTG). Thus, the inversion of high-precision gravity and gravity gradient data is urgently needed.

Conventional gravity inversion is a method of linear inversion or non-linear inversion to minimize the objective function based on the inversion theory and in the sense of least squares. A lot of efforts have been put into the research on the inversion of the gravity and the gravity gradient, which has been applied in determining the parameters of the geological model body, the depth, and fluctuation of the physical interface, and the density distribution(Hamzeh and Mehramuz, 2019; Li, 2018; Pedersen et al., 2019; Salem et al., 2013). Due to non-uniqueness, the geophysical inversion should be constrained by prior information, such as setting physical property

range, prior geological information, and inversion results from other geophysical methods(Hou et al., 2020; Zhou, 2014).

Density imaging is a method of directly calculating the sub-surface density distribution based on the gravity anomaly. The Cribb imaging method was based on the Fourier transform and calculated the density distribution in the sub-surface based on the vertical derivative of the observed gravity anomaly(Cribb, 1976). A density equivalent distribution method was proposed (Kobrunov and Varfolomeev, 1981), which converted the gravity data to data in the wavenumber domain based on Fourier transform and inverted the density distribution according to the spectrum of the gravity data. DEXP (depth from extreme points) imaging is a fast and stable method to predict the depth of abnormal objects through extreme points (Fedi, 2007). A 3D correlation imaging method of gravity anomaly and gravity gradient data was proposed, which provides good vertical and horizontal resolution for the spatial occurrence of abnormal geological bodies and the equivalent residual mass distribution(Guo et al., 2009). Priezzhev determined the geological model of the deeper part through rapid computation in the wavenumber domain and random iteration by combining with the prior information and using the gravity field data(Priezzhev, 2010). The iterative inversion method of gravity in the wavenumber domain based on functional representation was proposed, which obtains the sub-surface density distribution model and sub-surface structure model rapidly (Kobrunov, 2015). The wavenumber domain iterative method for rapid 3D imaging of gravity and gravity gradient data was proposed, introducing a depth scale factor to obtain a density model with fairly high resolution and accuracy(Cui and Guo, 2019).

A significant progress has been made in the previous study. Limited by observation methods, the previous studies were focused on the constraints on inversrion of the gravity and gravity gradient by introducing depth weighting or scale factors and iteration by using different iterative methods. There is no related research on the spectrum characteristics of the gravity gradient data. In this paper, the spatial anomaly of the gravity and gravity gradient data and the spectrum characteristics in the wavenumber domain of the theoretical model were analyzed. Based on the 3D density

imaging method of gravity in the wavenumber domain, a high-precision 3D density model was efficiently obtained. The measured gravity and gravity gradient data in the Decorah region of the United States was inverted to obtain the sub-surface high-precision 3D density model, verifying the effectiveness of the method.

2. Method

2.1. Gravity gradient forward modeling theory

According to Newton's law of gravitation, the gravitational potential $P(x_0, y_0, z_0)$ of a mass body with a certain volume in the earth at any point in space can be calculated:

$$\mathbf{U}(x_0, y_0, z_0) = \gamma \iiint_v \frac{\rho dv}{r} \tag{1}$$

where (x_0, y_0, z_0) is a point in the mass body, ρ is the density of the mass body at that point, dv is the volume element of the mass body, γ is the gravitation constant, r is the distance from the mass element to the computation point in the geological body.

Referring that the gravity anomaly is the vertical first-order partial derivative of the gravity potential, g_x, g_y and g_z represent the components of gravity in the X, Y, Z directions respectively(Pereira Bomfim, 2012), and the gravity gradient is the derivative of the first-order derivative of the gravity potential in three directions.

$$\bar{T} = \Delta U = \begin{bmatrix} \frac{\partial^2 U}{\partial x^2} & \frac{\partial^2 U}{\partial x \partial y} & \frac{\partial^2 U}{\partial x \partial z} \\ \frac{\partial^2 U}{\partial y \partial x} & \frac{\partial^2 U}{\partial y^2} & \frac{\partial^2 U}{\partial y \partial z} \\ \frac{\partial^2 U}{\partial z \partial x} & \frac{\partial^2 U}{\partial y \partial z} & \frac{\partial^2 U}{\partial z^2} \end{bmatrix} = \begin{bmatrix} \frac{\partial g_x}{\partial x} & \frac{\partial g_x}{\partial y} & \frac{\partial g_x}{\partial z} \\ \frac{\partial g_y}{\partial x} & \frac{\partial g_y}{\partial y} & \frac{\partial g_y}{\partial z} \\ \frac{\partial g_z}{\partial x} & \frac{\partial g_z}{\partial y} & \frac{\partial g_z}{\partial z} \end{bmatrix} = \begin{bmatrix} T_{xx} & T_{xy} & T_{xz} \\ T_{yx} & T_{yy} & T_{yz} \\ T_{zx} & T_{zy} & T_{zz} \end{bmatrix} \tag{2}$$

where, T_{pq} is the component of the gradient, and its second-order derivative satisfies the Laplace's equation, and $T_{xy} = T_{yx}$, $T_{xz} = T_{zx}$ and $T_{yz} = T_{zy}$. So only five components of the gradient are independent. Each gravity gradient component leads a unique response to the size, shape, and thickness of the density anomaly, providing extensive constraints during the interpretation.

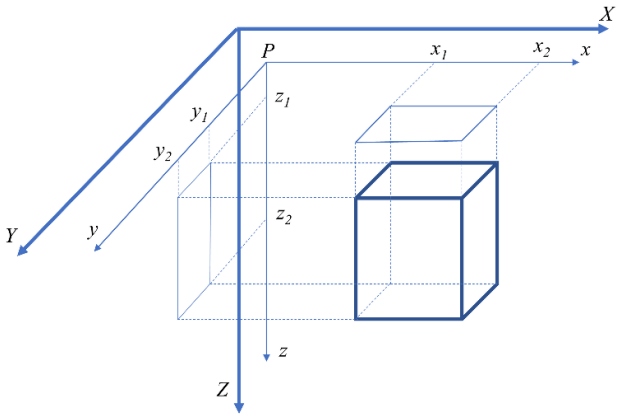

Fig. 1. Rectangular prism model

The gravity anomaly formula referring to the rectangular prism models expressed as (Blakely, 1995)(Fig.1):

$$g_z = \gamma\rho \int_{z_1}^{z_2} \int_{y_1}^{y_2} \int_{x_1}^{x_2} \frac{z}{\{(x-x_0)^2 + (y-y_0)^2 + (z-z_0)^2\}^{3/2}} dxdydz \tag{3}$$

The scope of the model, $x_1 \le x \le x_2$, $y_1 \le y \le y_2$ and $z_1 \le z \le z_2$.The result of g_z is as follows(Plouff, 1976):

$$g_z = \gamma\rho \sum_{i=1}^{2} \sum_{j=1}^{2} \sum_{k=1}^{2} \mu_{ijk} \left[z_k arcta\, n \frac{x_i y_j}{z_k R_{ijk}} - x_i lo\, g(R_{ijk} + y_j) - y_j log(R_{ijk} + x_i) \right] \tag{4}$$

where,

$$R_{ijk} = \sqrt{x_i^2 + y_j^2 + z_k^2}$$
$$\mu_{ijk} = (-1)^i (-1)^j (-1)^k$$

The second-order derivative of the gravity potential is expressed as:

$$T_{xx} = \gamma\rho \left\| \left| \arctan \frac{(x-x_0)R}{(y-y_0)(z-z_0)} \right|_{x_1}^{x_2} \right|_{y_1}^{y_2} \Big|_{z_1}^{z_2}$$

$$T_{xy} = \gamma\rho \| | \ln (z - z_0 + R) \Big|_{x_1}^{x_2} \Big|_{y_1}^{y_2} \Big|_{z_1}^{z_2}$$

$$T_{zz} = \gamma\rho \parallel \arctan \frac{(z-z_0)R}{(x-x_0)(y-y_0)} \Big|_{x_1}^{x_2} \Big|_{y_1}^{y_2} \Big|_{z_1}^{z_2} \tag{5}$$

$$T_{xz} = \gamma\rho \| | \ln (y - y_0 + R) \Big|_{x_1}^{x_2} \Big|_{y_1}^{y_2} \Big|_{z_1}^{z_2}$$

$$T_{yy} = \gamma\rho \left\| \left| \arctan \frac{(y-y_0)R}{(y-y_0)(z-z_0)} \right|_{x_1}^{x_2} \right|_{y_1}^{y_2} \Big|_{z_1}^{z_2}$$

$$T_{yz} = \gamma\rho \| | \ln (x - x_0 + R) \Big|_{x_1}^{x_2} \Big|_{y_1}^{y_2} \Big|_{z_1}^{z_2}$$

The gravity and gravity gradient are converted to obtain their spectrum in the wavenumber domain by Fast Fourier Transform(FFT), the spectrum of gravity anomaly is obtained(Priezzhev, 2010):

$$G(k_x,k_y)=\int_{-\infty}^{\infty}\int_{-\infty}^{\infty}g(x,y)e^{-i(k_xx+k_yy)}dxdy$$
$$g_z(x,y)=\frac{1}{4\pi^2}\int_{-\infty}^{\infty}\int_{-\infty}^{\infty}G(k_x,k_y)e^{i(k_xx+k_yy)}dk_xdk_y \quad (6)$$

where, $g_z(x,y)$ is the gravity anomaly, $G(k_x,k_y)$ is the spectrum of the gravity anomaly, k_x and k_y are the wavenumbers at *x*-axis and *y*-axis respectively. The formula of calculating the gravity gradients in the wavenumber domain is expressed as(Mickus and Hinojosa, 2001):

$$\Gamma_{ij}(x,y)=F^{-1}\{[K(k_x,k_y)G(k_x,k_y)]\}$$

where, $[K(k_x,k_y)]=\begin{bmatrix}\frac{-k_x^2}{|k|} & \frac{-k_xk_y}{|k|} & -ik_x\\ \frac{-k_xk_y}{|k|} & \frac{-k_y^2}{|k|} & -ik_y\\ -ik_x & -ik_y & |k|\end{bmatrix}$

The spectrum of the gravity gradients are obtained.

The SI unit of gravity is m/s^2, that of gravity gradient is Gal, and that of gravity gradient is $1/s^2$. Practically, the unit of gravity gradient is 1E (Eotvos) =10^{-9} $1/s^2$. The SI unit of gravity anomaly spectrum is $mGal\cdot m^2$, and the unit of gravity gradient spectrum is $E\cdot m^2$.

2.2. 3D density imaging theory of gravity and gravity gradient in the wavenumber domain

The vertical first-order derivative of the gravity potential in the point (x_0,y_0,z_0) and the density distribution of an area below the point satisfies the integral equation:

$$g_z=\gamma\iiint_v\frac{\rho(x,y,z)(z-z_0)}{\{(x-x_0)^2+(y-y_0)^2+(z-z_0)^2\}^{3/2}}dxdydz \quad (7)$$

where, g_z is the observation of gravity anomaly on the *z*=0 plane, $\rho(x,y,z)$ is the 3D density distribution. Calculate the spectrum in the wavenumber domain is expressed as(Priezzhev, 2010):

$$G(k_x, k_y) = 2\pi\gamma \int_{z=0}^{\infty} P(k_x, k_y, z) e^{-kz} dz \quad (8)$$

where, $G(k_x, k_y)$ is the spectrum of gravity anomaly, and $P(k_x, k_y, z)$ is the density spectrum of the horizontal zone at depth z.

Assuming that:

$$P(k_x, k_y, z) = Q(k_x, k_y) K(k_x, k_y, z) \quad (9)$$

where, $Q(k_x, k_y)$ is depth-independent, and $K(k_x, k_y, z)$ is depth-dependent. $Q(k_x, k_y)$ is expressed as:

$$Q(k_x, k_y) = \frac{1}{2\pi\gamma} \frac{G(k_x, k_y)}{\int_{z=0}^{\infty} K(k_x, k_y, z) e^{-kz} dz}$$

Then,

$$P(k_x, k_y, z) = \frac{1}{2\pi\gamma} \frac{K(k_x, k_y, z)}{\int_{z=0}^{\infty} K(k_x, k_y, z) e^{-kz} dz} G(k_x, k_y)$$

Which is the relationship between with density spectrum and gravity spectrum. the wavenumber domain inversion operator is expressed as:

$$H(k_x, k_y, z) = \frac{1}{2\pi\gamma} \frac{K(k_x, k_y, z)}{\int_{z=0}^{\infty} K(k_x, k_y, z) e^{-kz} dz}$$

Considering to eliminate the Gibbs phenomenon and generate smooth filter, $K(k_x, k_y, z)$ is defined as $z^n e^{-nkz}$.

Then,

$$H(k_x, k_y, z) = \frac{1}{2\pi\gamma} \frac{(n+1)^{n+1}}{n!} z^n k^{n+1} e^{-nkz}$$

The spectrum of the density distribution is expressed as:

$$P(k_x, k_y, z) = \frac{1}{2\pi\gamma} \frac{(n+1)^{n+1}}{n!} z^n k^{n+1} e^{-nkz} G(k_x, k_y, 0)$$

which is treated with inverse Fourier transform, we obtain:

$$\rho(x, y, z) = F^{-1}\left[\frac{1}{2\pi\gamma} \frac{(n+1)^{n+1}}{n!} z^n k^{n+1} e^{-nkz} G(k_x, k_y, 0)\right] \quad (10)$$

The formula for calculating the density distribution based on the gravity gradient

spectrum:

$$\rho(x,y,z) = F^{-1}\left[\frac{1}{2\pi\gamma}\frac{(n+1)^{n+1}}{n!}z^n k^{n+1}e^{-nkz}\frac{|k|}{-k_x^2}F\{T_{xx}(x,y,z)\}\right]$$

$$\rho(x,y,z) = F^{-1}\left[\frac{1}{2\pi\gamma}\frac{(n+1)^{n+1}}{n!}z^n k^{n+1}e^{-nkz}\frac{|k|}{-k_x k_y}F\{T_{xy}(kx,y,z)\}\right]$$

$$\rho(x,y,z) = F^{-1}\left[\frac{1}{2\pi\gamma}\frac{(n+1)^{n+1}}{n!}z^n e^{-nkz}\frac{k^{n+1}}{-ik_x}F\{T_{xz}(x,y,z)\}\right]$$

$$\rho(x,y,z) = F^{-1}\left[\frac{1}{2\pi\gamma}\frac{(n+1)^{n+1}}{n!}z^n k^{n+1}e^{-nkz}\frac{|k|}{-k_y^2}F\{T_{yy}(x,y,z)\}\right] \quad (11)$$

$$\rho(x,y,z) = F^{-1}\left[\frac{1}{2\pi\gamma}\frac{(n+1)^{n+1}}{n!}z^n e^{-nkz}\frac{k^{n+1}}{-ik_y}F\{T_{yz}(x,y,z)\}\right]$$

$$\rho(x,y,z) = F^{-1}\left[\frac{1}{2\pi\gamma}\frac{(n+1)^{n+1}}{n!}z^n e^{-nkz}k^n F\{T_{zz}(x,y,z)\}\right]$$

3. Forward modeling and inversion

3.1. Forward modeling of gravity and gravity gradient of rectangular prism model

To verify theoretically the relation between the gravity and gravity gradient and the model, model I is set up for simulation.

The gravity and the gravity gradient anomalies are related to the edge, boundary, angle, and mass center of the anomalous mass(Fig.2). By measuring the EW variation of gravity, the zero value of T_{xx} delineates the boundary in the *y*-direction. By measuring the NS variation of gravity, the zero value of T_{yy} delineates the boundary in the *x*-direction. The extreme value of T_{xy} corresponds to the corner point. T_{xz} depicts the anomalous axis in the NS direction, and its extreme value indicates the boundary in the *y*-direction. T_{yz} depicts the east-west anomaly axis in the EW direction, and its extreme value indicates the boundary in the *x*-direction. The extreme value of g_z and T_{zz} indicates the abnormal center. T_{zz} has a higher resolution ratio than Δg, and its zero value corresponds to the boundary.

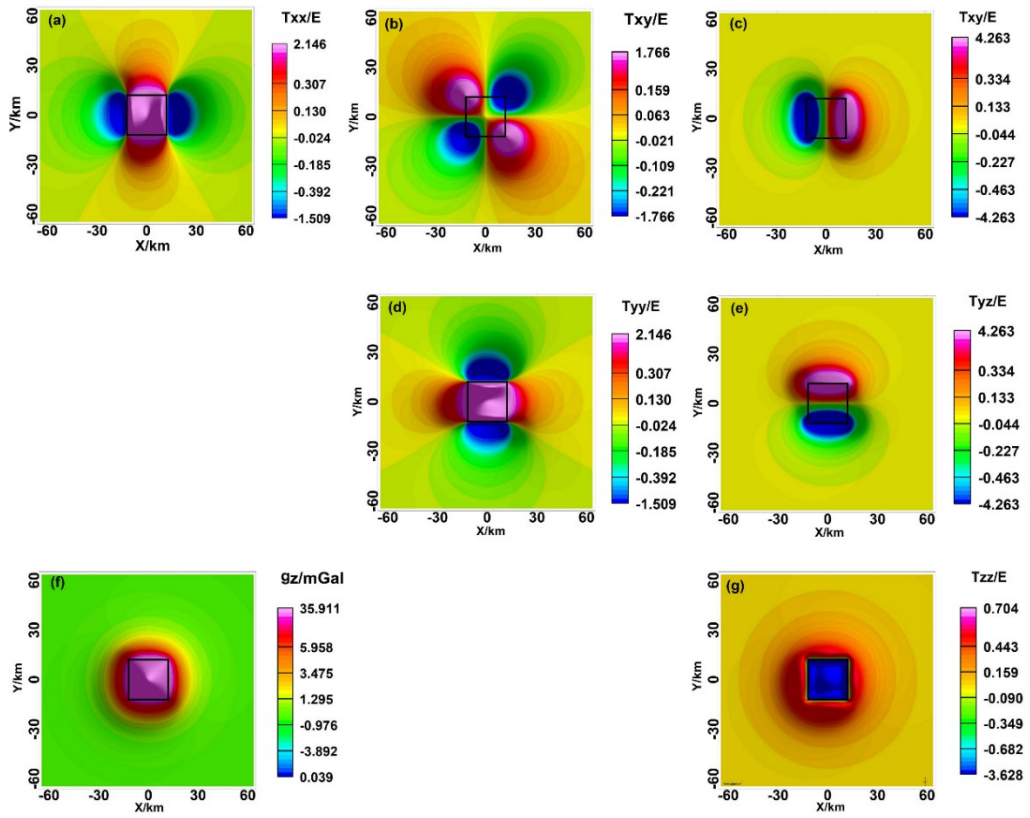

Fig. 2. Gravity and gravity gradient anomalies of Model I

(a) T_{xx} (b) T_{xy} (c) T_{xz} (d) T_{yy} (e) T_{yz} (f) g_z (g) T_{zz}, Blackline is the model

The spectrum of gravity anomaly shows obvious fluctuation and rapid attenuation, and the spectrum of the gravity gradient T_{zz} shows slower attenuation, more obvious periodicity, and obvious response in the k_x and k_y directions. Computation of the gravity anomaly spectrum and the analysis of spectrum characteristics show that the gravity anomaly spectrum function of the three-dimensional body is symmetry (He and Fang, 2020). The spectrum characteristics of the gravity gradient are closely related to the direction of each component. The spectrum functions of T_{xx} and T_{xy} show the characteristics of rapid attenuation, and the spectrum contours are parallel to the k_x direction. T_{xx} shows obvious periodic fluctuation at the k_x axis, and T_{yy} and T_{yz} shows obvious periodic fluctuation at the k_y axis. The T_{zz} spectrum shows the characteristics similar to those of the g_z spectrum, but stronger periodicity than g_z spectrum. The g_z spectrum shows rapid attenuation. According to the spectrum characteristics, the T_{xx} and T_{xy} spectra are not applicable in further inversion.

The amplitude spectrum is the variation of the amplitude of the gravity anomaly

spectrum with frequency, reflecting the distribution characteristics of the anomaly amplitude.

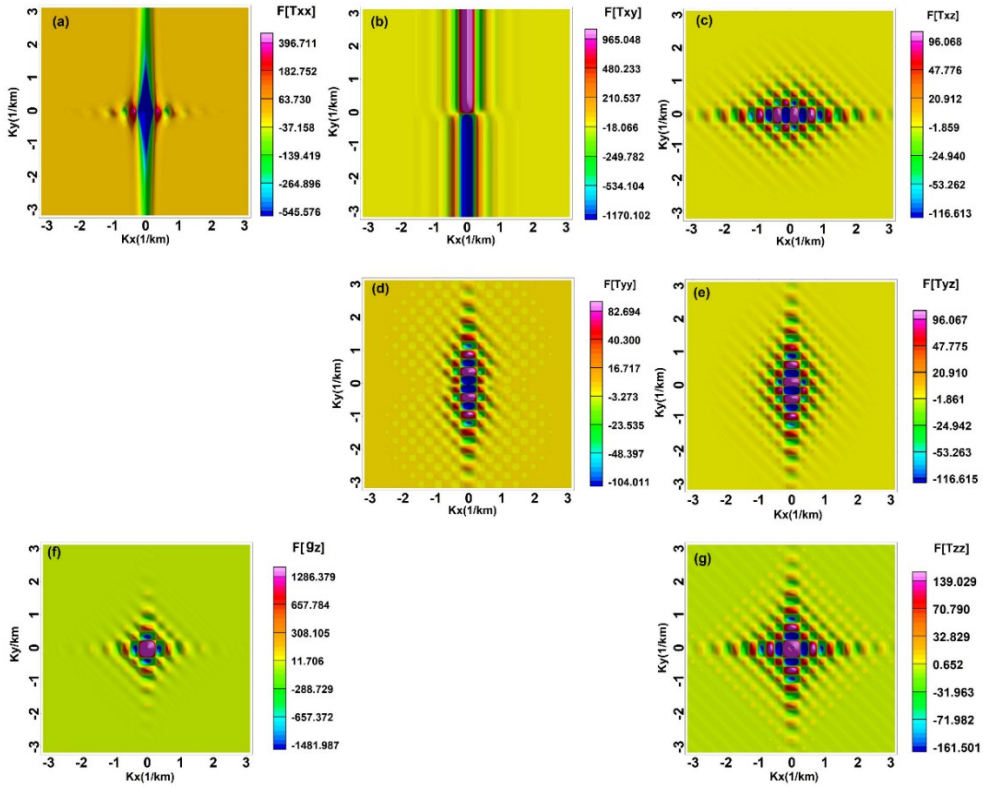

Fig. 3. The amplitude spectrum of the gravity gradient

(a)$F[\,T_{xx}]$ (b)$F[\,T_{xy}]$ (c) $F[T_{xz}]$ (d) $F[T_{yy}]$ (e) $F[T_{yz}]$ (f) $F[g_z]$ (g) $F[T_{zz}]$

The characteristics of the gravity anomaly and the gravity gradient amplitude spectrum are similar to their spectrum characteristics except for better periodicity (Fig.3). According to the periodic fluctuation characteristics of the amplitude spectrum, the model can be inverted to a rectangular prism, and the model half-width in the horizontal direction can be calculated from the wave value at the first minimum of the amplitude spectrum.

$$B = \frac{\pi}{\Delta w} \tag{12}$$

Due to the equivalence between the gravity anomaly spectrum function of the three-dimensional body and that of the two-dimensional body(Xiong, 1979), the profiles at k_y=0 of the gravity anomaly amplitude spectrum and the gravity gradient amplitude spectrum were extracted. Due to the small amplitude of the gradient amplitude spectrum, two profiles were extracted. According to the profile of the

amplitude spectrum, the first minimum points of the amplitude spectrum occur at the same position, corresponding to the wave value of 0.247. The model half-width was calculated as 12.7 km with Formula (12). The actual width is 12km. Analysis of spectrum characteristics shows the poor inversion of the spectrum signals of T_{xx} and T_{xy}.

The power spectrum, also known as the energy spectrum, is the square of the amplitude spectrum, the average radial power spectrum of E is obtained:

$$E = (r) = \frac{1}{2\pi}\int_{0}^{2\pi} E(r,\theta)d\theta \tag{13}$$

then, logarithmic the above formula to obtain the average radial logarithmic power spectrum,

$$ln\,E\,(r) = A - 2rh_t \tag{14}$$

where,A is a constant, and the above formula shows a straight line with slope of $-2h_t$:

$$h_t = -\frac{ln\,E\,(r_2) - ln\,E\,(r_1)}{r_2 - r_1} \tag{15}$$

It can be seen that the buried depth of the model can be calculated according to the slope of the average radial logarithmic power spectrum.

To verify the noise immunity of the density imaging method, the theoretical forward gravity and gravity gradient anomalies of Model II were computed(Fig.4), and 10% noise was added. Then, the effects of noise on the gravity and gravity gradient anomalies were analyzed.

The model boundary can't be clearly described with the gravity anomaly of the complex model, and the gravity gradient anomalies well coincide with the model boundary or the inflection point, especially the outline of the model position is clearly described with T_{zz} (Fig.5). While the gravity and gravity gradient data with noise-added characteristic lines are fuzzy. The anomaly basic characteristics corresponding to the model body are not significantly changed.

In addition, according to the comparative analysis of the calculation speed of model I and model II, it is verified that the forward modeling speed in the wavenumber domain is better than that in the spatial domain. When the number of models is large and complex, the calculation efficiency advantage in the wavenumber domain is greater,

which is more conducive to improving the inversion efficiency in the calculation of complex models(Table 1).

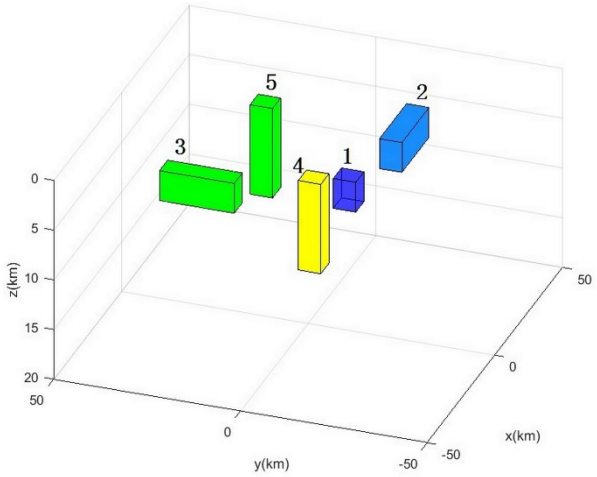

Fig. 4. Model II location

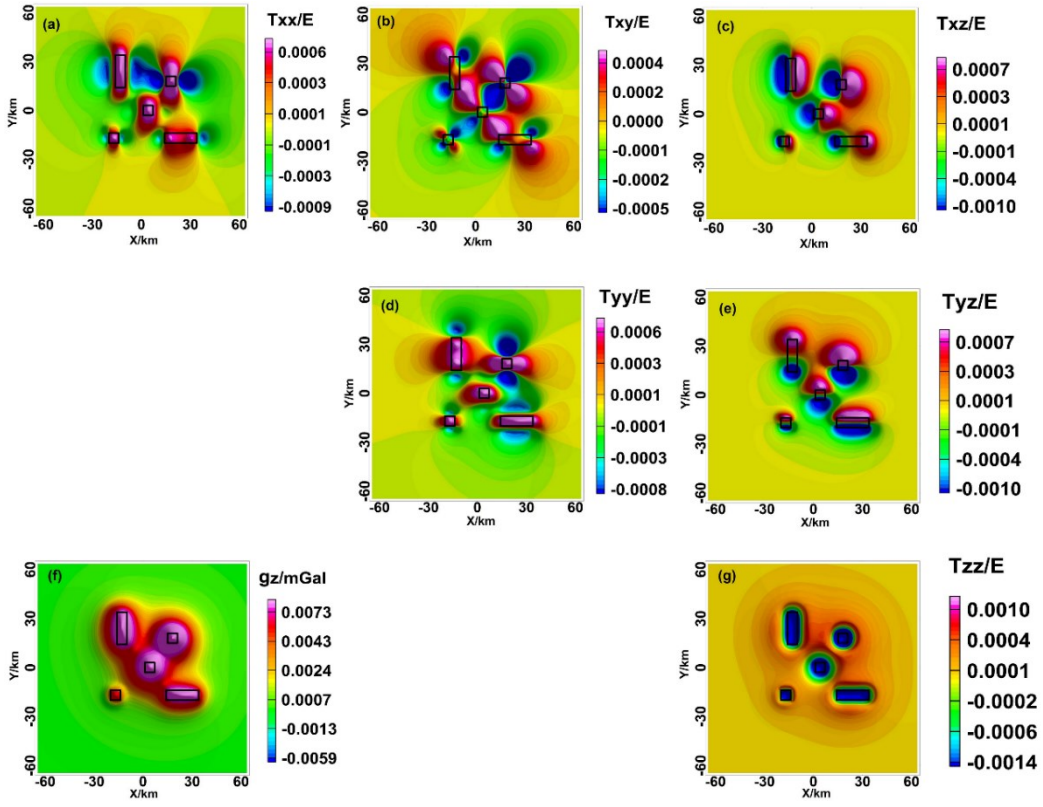

Fig. 5. Gravity and gravity gradient anomalies of Model II

(a) T_{xx} (b) T_{xy} (c) T_{xz} (d) T_{yy} (e) T_{yz} (f) g_z (g) T_{zz}, Blacklines are the models

Table 1. Comparison of forward modeling velocity of gravity and gravity gradient in space domain and wavenumber domain

	Forward velocity in space domain	Forward velocity in wavenumber domain	Forward modeling speed advantage in wavenumber domain
Model I	0.08s	0.03s	Increase by 62.5%
Model II	0.26s	0.05s	Increase by 80.7%

Note: The more complex the model is, the more obvious the velocity advantage in wavenumber domain is.

3.2. 3D density imaging in the wavenumber domain

The forward modeling data of the theoretical model and the noise-added data were inverted to verify the effectiveness and noise immunity of the method. First, preliminarily judge the depth and width of the model according to the spectrum of gravity,which is added to density imaging as constraint. In this paper, the depth weighting function proposed by Commer is introduced to improve the longitudinal resolution(*Commer*, 2011).

$$W(z) = \frac{\alpha + \exp\left[\frac{r_1}{dz}(z - z_{c1})\right]}{1 + \exp\left[\frac{r_1}{dz}(z - z_{c1})\right]} - \frac{\alpha + \exp\left[\frac{r_2}{dz}(z - z_{c2})\right]}{1 + \exp\left[\frac{r_2}{dz}(z - z_{c2})\right]} \tag{16}$$

where,z is the center depth, dz is inverse domain, α is empirical value, $\alpha = 0.001$, z_{c1}, z_{c2} are the depth of the top and bottom of the model. r is the interface constraint factor.The iterative inversion formula with the depth weighting function shows following:

$$\rho_{i+1} = \rho_i + W(z) \times \Delta\rho \tag{17}$$

Then, the sub-surface space to be inverted is divided into *N* horizontal layers, where each layer is divided into $m \times n$ rectangular prisms. The rectangular prism in each layer is iterated according to Formulas (10) and (17). The iteration process is as follows(where, $\rho_0 = 0$):

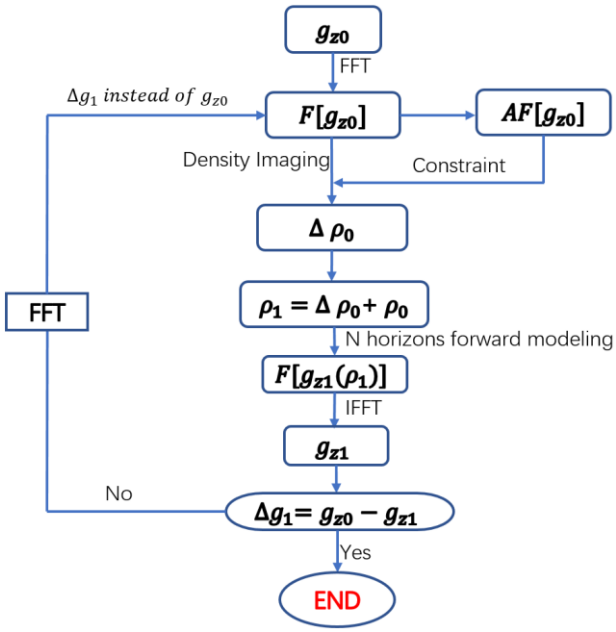

Fig.6 Density imaging iteration flowchart

First, the density imaging computation of Model II in Table 1 in the wavenumber domain was performed. The 3D density imaging results of gravity g_z and gravity gradient T_{zz} show in Fig.7. According to the theoretical models, the inversion effects of two sets of data are perfect, and the positions of five theoretical models can be located. The horizontal positions of the inversion results of two sets of data show in Fig.7a and 7b, where the black boxes are the actual positions of models, and the outline of the model boundaries are clearly described. The vertical profile of the data inversion results was shown in Fig.7c and 7d, the position of the anomaly body from two sets of data is consistent with the positions of the model. Due to the higher density in Model 4, a certain tailing phenomenon occurs in Model 5.

The 3D density imaging results of other components of the gravity gradient shows less false anomaly compared with the 3D density imaging of g_z and T_{zz}. Affected by the derivative of the data, the false anomalies from T_{xx} and T_{xz}, T_{yy} and T_{yz}, and T_{xy} in the *x*-directin, *y*-direction, in *x* & *y*-directions.The 3D density imaging results of g_z and T_{zz} are significantly better than those of other gravity gradients. Therefore, g_z and T_{zz} were selected for further analysis and inversion.

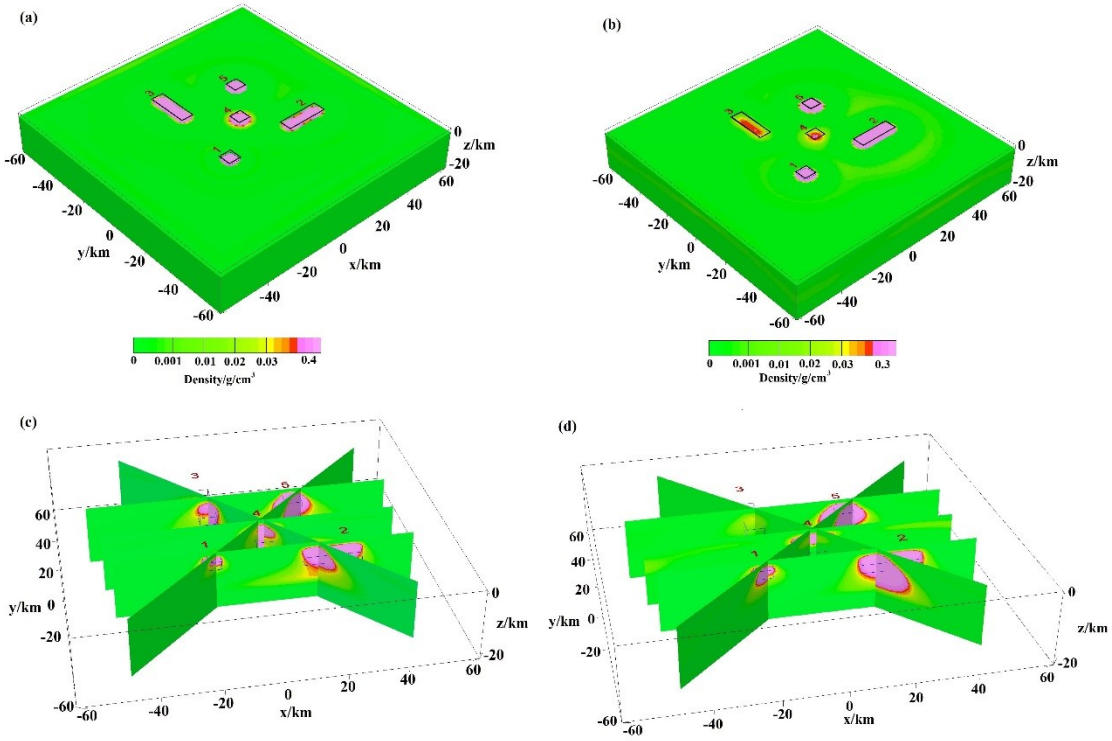

Fig. 7. g_z/T_{zz} 3D density imaging results

(a) cross-section at z=-2 ;(b) cross-section at z=-2; (c) slices of (a);(d) slices of (b)

The noise was added to g_z and T_{zz} data to perform 3D density imaging to understand the noise immunity of the method. The noise-added 3D density imaging results of g_z and T_{zz} are still consistent with those of the actual model. The high-density values are concentrated in the model area. The evaluation results of the density imaging shows the forward modeling value of the inverted density model is very close to the residual error of the theoretical value, which proves the strong noise immunity of the method. The method was applied to the Decorah region of the United States to further verify its effectiveness.

4. Verification with measured data

The Decorah area is rich in mineral resources, and the area is a large area of sediments. Bell Geospace has carried out high-precision gravity and gravity gradient measurements in this area, and the high-precision full tensor data of gravity and gravity gradient are collected. The 3D density imaging in the wavenumber domain method is used to obtain the sub-surface 3D density distribution. The effectiveness of the method

was verified.

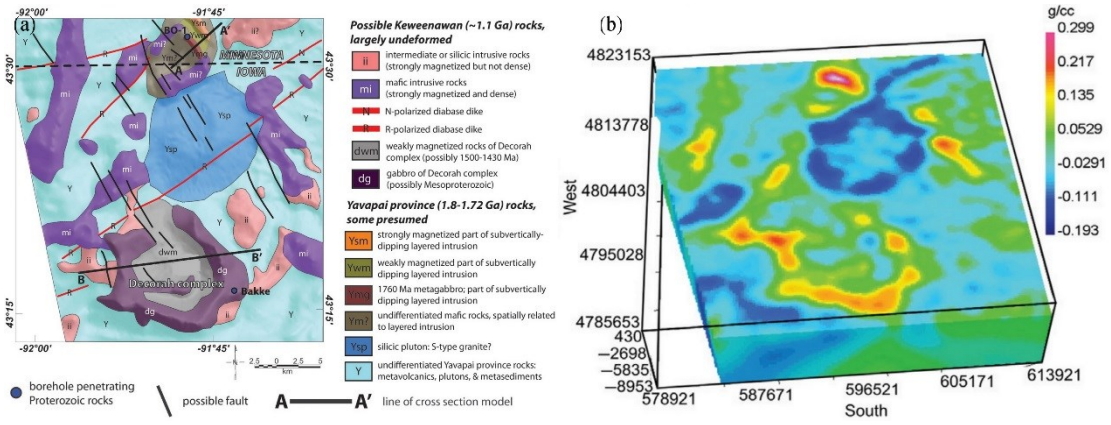

Fig. 8. Decorah

(a) Geologic map (Drenth et al., 2015) **(b)** 3D density model(Sun et al., 2020)

Both gravity and gravity gradient anomalies are caused by density differences, which reflect variation in the density of materials inside the earth. Gravity gradient anomalies are sensitive to the variation in shallow density differences, and the gravity anomaly reflects the information of deep field sources. Thus, the density distribution in the whole area can be obtained by comparing the gravity anomaly with the gravity gradient anomalies. Gaussian filtering is used to remove the influence of the sedimentary caprock in this area to obtain the gravity and gravity gradient anomalies of the target. The study area is also called the northeastern Iowa intrusive complex area(Drenth et al., 2015; Sun et al., 2020). The southern part of this area is the Decorah complex, which is a relatively dense mafic intrusive rock, and the middle part is a relatively low-density siliceous intrusion. Some small, relatively dense, mafic, or siliceous rocks intruded into the relatively low-density surrounding rocks.

The data from the study area was measured by Bell GeoSpace from December 2012 to January 2013 with the gravity full tensor gradient measurement system in the aerial surveys. The data cover 94 EW survey lines with a spacing of 400 m and 9 connecting lines with a spacing of 4000m. The gravity and gravity gradient anomalies show in Fig .9a and 10b. According to g_z, there is a large range of low gravity anomalies in the northeast of the study area, which corresponds to the siliceous intrusion, combined with the geological map (Fig .8a). There are several traps of

anomaly high value and a high-value anomaly belt in the north-to-east direction on the west side of the study area, a small range of anomaly high value in the northern part, and a large range of high value and high amplitude from the southwest side to the south side. The high amplitude reflects the location of the Decorah Complex. There are also several local anomalies, which are more obvious in T_{zz} map, where the anomaly high-value area is highlighted in the east part, and the abnormal outline of the high-value area is clear in the south part. Several high-value anomalies with small amplitudes occur in the areas where the changes are relatively flat. Combining with the analysis of gravity and gravity gradient, the study area was divided into several structural units.

According to the above analysis, density imaging was performed using gravity anomaly g_z and gravity gradient T_{zz}, with the sub-surface inversion at the depth of 0-8km, the interval of 150m between layers, 20 times of iteration, the sub-surface model grid points of (930×997×53) (Fig .9).

The horizon of the 3D density body at the depth of 1250m in the region was obtained by the Tikhonov regularization inversion method based on smoothness (Fig .8b). The horizon at the same depth of the 3D density body calculated by the method in this paper shows in Fig .9c and 9d. The two density models are consistent, but there are some minor differences. Combining with the analysis of the Geologic map of Decorah, there is an anomaly body with a relatively large range and low density in the central part to the northeast, revealing the location of the siliceous intrusive rock due to some extension to the northeast direction. Two anomaly bodies with a relatively small range and high density in the east and north sides are the mafic intrusion body. The intrusion body on the east side shows a nearly NS trend. The anomaly body with a relatively high density occurs both on the west and southwest sides. A large-scale SW trending Decorah complex occurs on the south side. The variation in the sub-surface 3D density structure in the study area is clearly illustrated to illustrate the variation process of the vertical profile. The intrusion process of the intrusion body from the bottom to the top illustrates visually. When the intrusion body reaches grid at the 2km, it gradually expands until the shallow layer is gradually covered by the sediments. The iso-surfaces of the density model inverted based on g_z and T_{zz} (Fig. 9e and 9f),

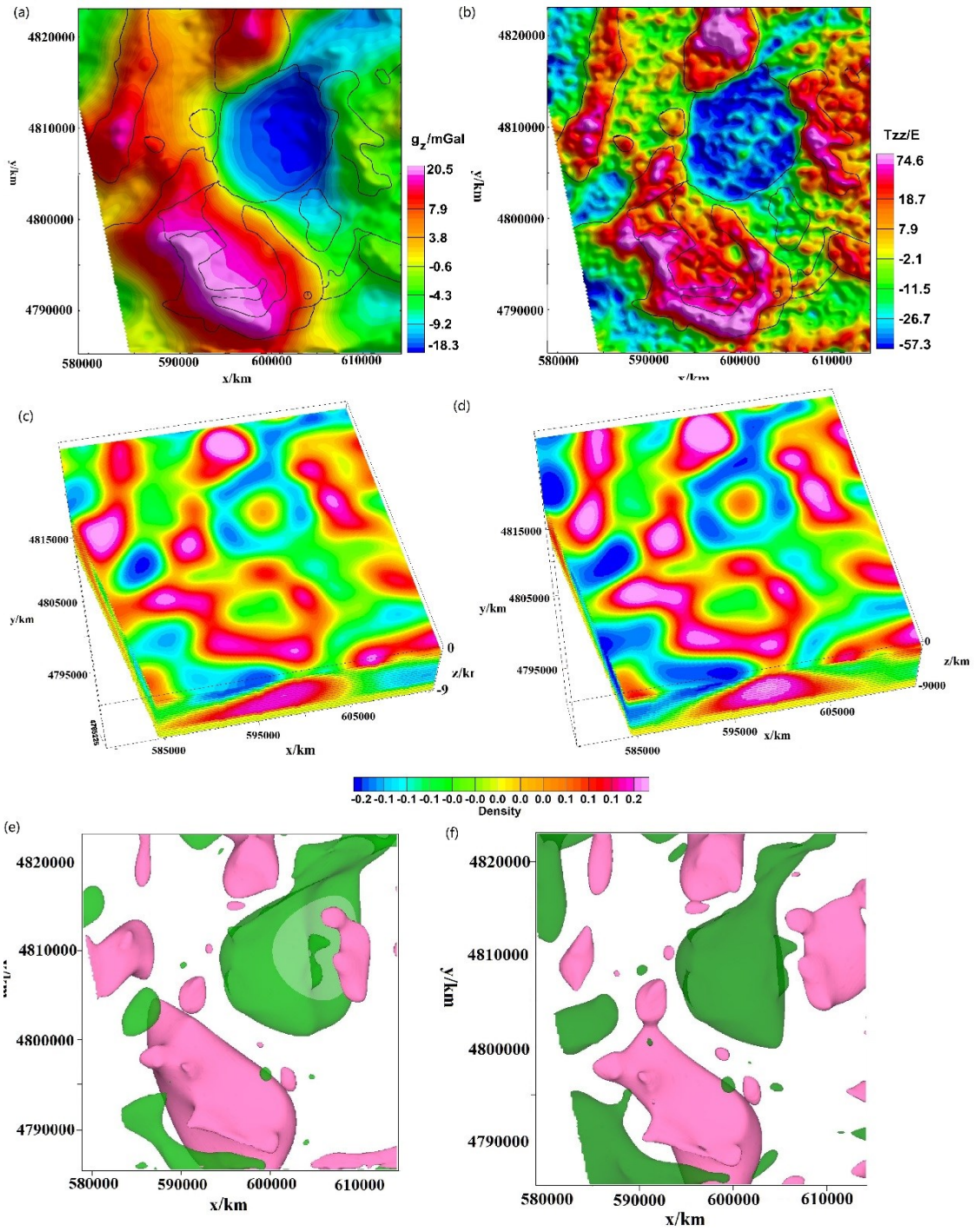

Fig. 9. Measured gravity and gravity gradient anomalies in Decorah

Blacklines are tectonic lines

(a) g_z (c) density voxel (e) isosurfaces（pick: ρ=0.11, green: ρ=-0.1）of g_z ;

(b) T_{zz} (d) 3D map (f) isosurfaces（pick: ρ=0.2, green: ρ=-0.18）of T_{zz}

and they correspond to the geological structural units (Fig .8b). The green area is the siliceous intrusion with the small relative anomaly. The red area is the high-density Ferro-magnesia intrusive rocks with a large relative anomaly. Except for the obvious anomaly areas analyzed above, some small anomaly areas can also be observed.

Through comparison and analysis, a high-precision 3D density model of the study area was obtained with the 3D density imaging method in the wavenumber domain, which provides a good method for further understanding of the geological distribution and mineral resources in this area.

5. Conclusions

In this paper, the characteristics of the gravity and gravity gradient anomalies in the spatial domain and the wavenumber domain were analyzed. The high-precision 3D sub-surface spatial density model was obtained with the 3D density imaging method in the wavenumber domain, and the effectiveness of the method was verified in the actual measurement area. Based on the characteristics of fast and highly efficient computation of the gravity and gravity gradient in the wavenumber domain, the computation of the 3D density imaging of the gravity and gravity gradient in the wavenumber domain was realized. According to the test of the model, and combined with the analysis of the spectrum characteristics, it is concluded that T_{zz} has a higher value of 3D density imaging inversion, and the inverted 3D density model is consistent with the theoretical model and shows strong noise immunity. Depth weighing improves depth imaging effect.Finally, the 3D density imaging inversion was performed with the gravity and gravity gradient T_{zz} in the Decorah area of the United States, and the distribution of intrusive rocks with different relative densities and the intrusion path of the rocks mass was obtained, verifying the effectiveness of the 3D density inversion method in the wavenumber domain, and guide further research in this area. The next step is to focus on maximizing the superiority of gravity and gravity gradient, performing joint inversion by mutual constrain, and improving the accuracy of the sub-surface 3D density model.

Acknowledgments

Thanks to Bell Geospace for full tensor gravity gradient data. This work was supported by the National Key R&D Program of China (grant number 2016YFC0601101), the National Natural Science Foundation of China (grant numbers 41874096), and the Strategic Pioneer Science and Technology Special Project of the Chinese Academy of Sciences (grant numbers XDB18010304), and the Basic Frontier Science Research Program of Chinese Academy of Science(grant numbers ZDBS-LY-DQC028), and the Independent Project of State Key Laboratory of Geodesy and Earth's Dynamics(grant numbers S21L6401).

Declaration of Competing Interest

The authors declare that they have no known competing financial interests or personal relationships that could have appeared to influence the work reported in this paper.

References

Blakely, R. J. (1995), Potential Theory In Gravity And Magnetic Applications, Stanford-Cambridge Program.

Commer, M. (2011), Three-dimensional gravity modelling and focusing inversion using rectangular meshes, *Geophysical Prospecting*, 59(5), 966-979.doi: 10.1111/J.1365-2478.2011.00969.X

Cribb, J. (1976), Application of the Generalized Linear Inverse to the Inversion of Static Potential Data, *Geophysics*, 41(6), 1365-1369.doi:10.1190/1.1440686

Cui, Y., and L. Guo (2019), A Wavenumber-Domain Iterative Approach for Rapid 3-D Imaging of Gravity Anomalies and Gradients, *IEEE Access*, 7, 34179-34188.doi: 10.1109/ACCESS.2019.2904717

Drenth, B. J., R. R. Anderson, K. J. Schulz, J. M. Feinberg, V. W. Chandler, W. F. Cannon, and R. Enkin (2015), What lies beneath: geophysical mapping of a concealed Precambrian intrusive complex along the Iowa–Minnesota border, *Canadian Journal of Earth Sciences,* 52(5), 279-293.doi:10.1139/CJES-2014-0178

Fedi, M. (2007), DEXP: A fast method to determine the depth and the structural index of potential

fields sources, *Geophysics*, 72(1), I1-I11.doi: 10.1190/1.2399452

Guo, L. H., X. H. Meng, L. Shi, and S. L. Li (2009), 3-D correlation imaging for gravity and gravity gradiometry data, *Chinese Journal of Geophysics-Ch*, 52(4), 1098-1106.doi: 10.3969/J.ISSN.0001-5733.2009.04.027

Hamzeh, A., and M. Mehramuz (2019), The depth estimation of subsurface anomalies using probability tomography imaging method from airborne vertical gravity gradient, *Journal of African Earth Sciences*, 149, 207-214.doi:10.1016/J.JAFREARSCI.2018.08.009

He, H., and J. Fang (2021), Research and Application of Gravity Anomaly Spectrum Analysis Method, *Geomatics and Information Science of Wuhan University*.doi: 10.13203/J.WHUGIS20200510

Hou, Z., Y. Zheng, E. Gong, and H. Cheng (2020), Joint Correlation Imaging Inversion with Gravity GradiometryData Based on Depth Weighting, *Journal of Northeastern University(Natural Science)*, 41(11), 1628-1632.doi:10.12068/J.ISSN.1005-3026.2020.11.017

Kobrunov, A. I., and V. A. Varfolomeev (1981), One approach of density equivalent representation and using it for gravity field interpretation, *Earth Physics USSR Academy of science*, 10.

Kobrunov, A. I. (2015), The method of functional representations in the solution of inverse problems of gravimetry, Izvestiya, *Physics of the Solid Earth*, 51(4), 459-468.doi: 10.1134/S1069351315030076

Li, H. (2018), Three-Dimension Crustal and upper Mantle Density Structure beneath the Qinghai-Tibet Plateau and its Adjacent Area, Ph.D thesis, Institute of Geodesy and Geophysics, Chinese Academy of Sciences.

Martinez, C., Y. Li, R. Krahenbuhl, and M. Braga (2010), 3D Inversion of airborne gravity gradiomentry for iron ore exploration in Brazil, *seg technical program expanded abstracts*.doi: 10.1190/1.3513181

Mickus, K. L., and J. H. Hinojosa (2001), The complete gravity gradient tensor derived from the vertical component of gravity: a Fourier transform technique, Journal of Applied *Geophysics*, 46(3), 159-174.doi:10.1016/S0926-9851(01)00031-3

Pedersen, L. B., J. Kamm, and M. Bastani (2019), A priori models and inversion of gravity gradient data in hilly terrain, *Geophysical Prospecting*, 68(3), 1072-1085.doi:10.1111/1365-2478.12897

Pereira Bomfim, E. (2012), The use of the Goce mission data for characterizations and implications

472 on the density structure of the sedimentary basins of amazon and solimoes, Brasil, *università*
473 *degli studi di trieste*.
474 Plouff, D. (1976), Gravity and Magnetic Fields of Polygonal Prisms and Application to Magnetic
475 Terrain Corrections, *Geophysics*, 41(4), 727-741.doi:10.1190/1.1440645
476 Priezzhev, I. (2010), Spectral and statistical analyses of aero geophysical data in system ASOM-
477 AGSES.pdf, Moscow State Geological Prospecting Academy.
478 Salem, A., S. Masterton, S. Campbell, J. D. Fairhead, J. Dickinson, and C. Murphy (2013),
479 Interpretation of tensor gravity data using an adaptive tilt angle method, *Geophysical*
480 *Prospecting*, 61(5), 1065-1076.doi: 10.1111/1365-2478.12039
481 Sun, J., A. T. Melo, J. D. Kim, and X. Wei (2020), Unveiling the 3D undercover structure of a
482 Precambrian intrusive complex by integrating airborne magnetic and gravity gradient data into
483 3D quasi-geology model building, *Interpretation*, 8(4), SS15-SS29.dou:10.1190/INT-2019-
484 0273.1
485 Vasco, D. W., and C. Taylor (1991), Inversion of airborne gravity gradient data, southwestern
486 Oklahoma, *Geophysics*, 56(1), 90-101.doi:10.1190/1.1442961
487 Xiong, G. (1979), On the theory about the relationship between the spectrums of the magnetic and
488 gravity anomalies of 2-D bodies and those of 3-D bodies, *Chinese Journal of Geophysics-Ch*
489 (04), 406-414.
490 Zhou, W. (2014), The study on rapid interpretation techniques of gravity anomaly and gravity
491 gradient tensor data, Ph.D thesis, Jilin University.